Soft Matter

View Online
Dynamic Article Links

Cite this: *Soft Matter*, 2011, **7**, 8050

www.rsc.org/softmatter

**PAPER**

# Heterogeneous crystallization of hard-sphere colloids near a wall

**Kirill Sandomirski,[a] Elshad Allahyarov,[bcd] Hartmut Löwen[b] and Stefan U. Egelhaaf*[a]**

***Received 25th February 2011, Accepted 27th May 2011***
**DOI: 10.1039/c1sm05346a**



We investigate the most basic situation of heterogeneous crystallization: crystallization of hard-sphere colloids in the presence of a flat hard wall. Using a combination of confocal microscopy and nonequilibrium Brownian dynamics simulations, microscopic time-resolved information is obtained on an individual-particle level. Initially, particles near the wall rearrange before an extended regime of crystal growth is found. During growth, we can directly observe a depletion zone in the fluid next to the progressing crystal–fluid interface due to the single-particle information provided by microscopy and simulations. This also allows us to follow the relaxation of the crystal layers and the progression of the crystal–fluid interface. In good agreement between our experiments and simulations, as well as previous studies, the growth rate shows a maximum in its dependence on the bulk volume fraction.

## 1 Introduction

Disorder–order transitions are central in statistical physics and highly relevant in determining material properties. Of special current interest are their kinetics and pathways, with crystallization being the classical example. Understanding the crystallization of an undercooled or over-compressed melt is not only important from a fundamental point of view[1–5] but is also relevant for many applications ranging from metallurgy[6] and material science, where, *e.g.*, one strives to create optical band-gap crystals,[7] to biology and biotechnology, where the crystallization of proteins is an important issue.[8–13] To identify the underlying processes, bulk methods have mainly been applied.[1,14,15] To make further progress, microscopic information on the particle level is also required. This can be provided through the investigation of colloidal suspensions, which have proven to be powerful model systems to study phenomena in statistical physics.

Recently several studies have been devoted to the homogeneous crystallization of bulk fluids.[1–3,14–17] The structure of the critical nuclei has been investigated by real-space experiments with colloidal suspensions[2,17–20] and computer simulations.[16,21,22] The nucleation rates have also been determined experimentally[1,2,17] and predicted theoretically[21] without full agreement being achieved yet.

Homogeneous crystallization is dominated by heterogeneous crystallization in many cases. Container walls and impurities are almost omnipresent and render heterogeneous crystallization especially relevant, often even inevitable, in practical situations and technical applications. Heterogeneous nucleation is induced by flat or curved walls,[3,23] structured walls,[24,25] individual seed particles[26–28] or particle assemblies.[29] Despite its importance, heterogeneous crystallization is less studied and understood than homogeneous nucleation. In particular, only a few experiments reveal the evolution of the crystalline structure on a particle level.[30,31]

We investigate the most basic realization of heterogeneous crystallization: heterogeneous crystallization near a flat hard wall in a suspension of colloidal hard spheres. Using confocal microscopy and Brownian dynamics simulations, we can follow the positions of individual particles. In good agreement between our experiments and simulations we find three consecutive regimes. Initially, particles near the wall rearrange. Subsequently the crystal grows and a depletion zone develops in the fluid ahead of the crystal–fluid interface. The crystal–fluid interface, whose width we can determine, propagates into the fluid. The rate of crystallization is found to exhibit a maximum upon increasing bulk volume fraction. Eventually crystal growth is observed to slow down and the crystal layers expand slightly.

The time scales of the first two regimes, rearrangement and crystal growth, are well separated. Because no appreciable nucleation barrier exists,[32,33] nucleation is very fast, while crystal growth progresses slowly. Heterogeneous nucleation and rearrangements are therefore essentially completed prior to the growth regime, which hence is unaffected by other processes. Furthermore, due to the simple, effectively one-dimensional geometry we avoid curvature effects. Together with the very basic situation, namely hard-sphere interactions and a flat hard wall, this allows us to investigate crystal growth without complications arising from other effects. We can thus obtain detailed quantitative information on crystal growth on a microscopic, individual-particle level. In particular, during crystal

[a]*Condensed Matter Physics Laboratory, Heinrich Heine University, 40225 Düsseldorf, Germany. E-mail: Stefan.Egelhaaf@uni-duesseldorf.de*
[b]*Institute for Theoretical Physics II, Heinrich Heine University, 40225 Düsseldorf, Germany*
[c]*Department of Physics, Case Western Reserve University, Cleveland, 44106, Ohio, USA*
[d]*Joint Institute for High Temperatures, Russian Academy of Sciences (IVTAN), 125412 Moscow, Russia*

growth we can directly observe a depletion zone which develops in the fluid ahead of the crystal–fluid interface.

## 2 Materials and methods

### 2.1 Samples and confocal microscopy

We use polymethylmetacrylate (PMMA) spheres, sterically stabilized by a thin (about 10 nm) layer of chemically grafted poly(12-hydroxystearic acid) (PHSA) and fluorescently labelled by 4-methylamino ethylmethacrylate-7-nitrobenzo-2-oxa-1,3-diazol (NBD). Using static and dynamic light scattering, their diameter is found to be $\sigma = 1.83$ μm with a polydispersity of less than 4%. They are suspended in a mixture of *cis*-decalin and cycloheptylbromide (CHB) to match their density; during 10 h of centrifugation at 4200 *g* no sedimentation was observed. This solvent mixture furthermore has a refractive index close to the one of the particles, which reduces van der Waals interactions and renders samples of 1 cm thickness still visually transparent. To reduce and screen the particles' charges, we use distilled and water-free solvents and add salt (tetrabutylammonium chloride, TBAC). Samples with volume fractions $0.50 \leq \Phi \leq 0.56$ are prepared by diluting a stock solution. The stock solution is a random close packed sediment created by centrifugation with an assumed $\Phi = 0.64$.[34] This value is consistent with the mass of dried samples and the number density determined by confocal microscopy. About 0.3 ml of the samples are kept and imaged in glass vials with a diameter of about 1 cm whose bottom is replaced by a microscope cover slide, which is used for imaging and represents the flat hard wall.[35] In contrast to smaller cells, such as capillaries, these vials allow us to melt crystals prior to each measurement using a small magnetic bar and thus to repeat measurements with the same sample. Independent of the melting procedure, however, next to the wall between one and about five layers are observed to be partially hexagonally ordered immediately after mixing, that is as soon as convective currents caused by mixing have decayed sufficiently and meaningful confocal microscopy images can be taken. If the sample is 'slowly' mixed so that simultaneous imaging is possible, we observe next to the wall a collective motion of parts of the layers, *i.e.* mixing on the length scale of a few particles rather than individual particles. We cannot detect whether thorough mixing leads to disorder on an individual particle level with a subsequent fast ordering or to disorder on the scale of a few particles. It has already previously been reported that partially ordered layers remain after mixing[1] which has been attributed to the favourable wetting of a flat hard wall by hard spheres.[32,33] Thus, at the beginning of individual imaging runs this order already exists in the otherwise melted samples. Since the specific order in the initial layers with grain boundaries and defects strongly affects the subsequent growth, we choose the observation volume such that in this region the wall is covered with only a single domain. Following this procedure, we achieve well-defined initial conditions and obtain reproducible results.

The particles are imaged using an Olympus FluoView FV1000 confocal microscope equipped with an Ar ion laser operated at a wavelength of 488 nm and connected to an Olympus IX81 inverted microscope with an 1.35 NA 60× oil-immersion objective. Confocal images are usually recorded at a distance of 10–70 μm from the cover slide. Since the wall is hence not in the field of view during kinetic runs, the start time is estimated by extrapolation and comparison with the simulations. It takes about 5 min to scan a sample volume of $96 \times 96 \times 60$ μm$^3$, corresponding to $512 \times 512 \times 300$ pixels and containing $N \approx 90\,000$ particles. Scans are recorded every 10 min for typically 3 h. Pixel noise in the images is removed using a software real-space bandpass filter. Subsequently, the positions of the local intensity maxima in the images, corresponding to individual particles, are determined.[36] We thus obtain the same kind of information as provided by simulations.

### 2.2 Brownian dynamics simulations

Our Brownian dynamics simulations are similar to those previously reported.[37] The simulations do not include hydrodynamic interactions, which, in concentrated suspensions, are believed to be negligible compared to the direct particle–particle interactions. The short-time infinite-dilution diffusion coefficient $D_0$ sets the Brownian time scale $\tau_B = \sigma^2/D_0$, in our experimental system $\tau_B = 37$ s. The simulation box contains $N = 80\,000$ hard spheres and has a rectangular shape with dimensions $L_x \times L_y \times L_z = 40.8\sigma \times 43.2\sigma \times \sim 45\sigma$, where $42\sigma \leq L_z \leq 49\sigma$ is adjusted to produce the desired volume fraction $\Phi$ in the range $0.50 \leq \Phi \leq 0.57$. Periodic boundary conditions are employed in the $x$ and $y$ directions, while two hard walls are located at $z = 0$ and $z = L_z$. Next to the wall at $z = 0$ we place a triangular layer of fixed spheres with a lattice constant $a = 1.133\sigma$, corresponding to a line spacing of $0.921\sigma$. Tests covering a range of lattice constants, $1.01\sigma \leq a \leq 1.60\sigma$, showed that about this spacing develops after about six layers, regardless of the spacing in the first, fixed layer and the volume fraction $\Phi$, with all the relevant $\Phi$ in the coexistence region. In these first about six layers a large number of defects exist for fixed lattice spacings $a \neq 1.133\sigma$, and beyond the first six layers the systems adopt a lattice spacing $a \approx 1.133\sigma$. Crystal growth starts at the wall located at $z = 0$, while, within the explored time window, crystallization is not detected at the bare wall at $z = L_z$, where it is considerably slower than on the structured wall. This mimics the experimental situation, where the bottom layers are observed to be ordered as soon as confocal images can be taken after the cessation of thorough stirring.

The initial configuration of non-overlapping, randomly arranged particles is prepared by random insertions of spheres. To avoid particle jamming in our highly concentrated suspensions, particles are sequentially inserted into layers, with the volume between the lower and top walls divided into 200 layers. Simulations were run for $1000\tau_B$ with time steps of $0.001\tau_B$. To improve statistics, for each condition, *i.e.* $\Phi$, several simulation runs were performed with different initial configurations. The initial configuration does not significantly affect our results, in particular the crystal growth regime remains unchanged with a depletion zone developing for all initial configurations investigated. In contrast, the initial nucleation regime is affected, with its duration changing by about $2\tau_B$.

### 2.3 Data analysis

Based on the particle positions, which are obtained from confocal microscopy or simulations, the local orientational-order

parameter $\vec{q}_6(i)$ is calculated for each particle $i$.[38,39] Two neighbouring particles $i$ and $j$, where particles are declared neighbours if their centres are within $1.17\sigma$ (similar results are obtained for larger values, *e.g.* $1.3\sigma$), are considered connected in a crystalline cluster, if $\vec{q}_6(i)\cdot\vec{q}_6(j) \geq 0.5$. (In a perfect fcc crystal by construction $\vec{q}_6(i)\cdot\vec{q}_6(j) = 1$.) If a particle has at least 8 connected neighbours, it is considered a crystalline particle.

The particle positions are also used to obtain the local volume fraction $\varphi(z, t)$. To calculate $\varphi(z, t)$, the sample is divided in the $z$ direction into bins of size $0.1\sigma$ and the number of particle centres in each bin determined, so that, for a perfect crystal, $\varphi(z, t)$ can show sharp peaks with heights reaching values far beyond unity. For a direct comparison with the bulk volume fraction $\Phi$, we calculate the locally-averaged volume fraction $\bar{\varphi}(z,t)$ by averaging the local volume fraction $\varphi(z, t)$ over $z_0 = 0.921\sigma$, corresponding to one period of the oscillations or one layer in the crystalline phase, and, furthermore, over a time interval of $3\tau_B$. Since we have determined the crystalline and fluid character of the particles, using the above-mentioned criterion, we can separately determine the local volume fractions $\varphi_c(z, t)$ and $\varphi_f(z, t)$ and locally-averaged volume fractions $\bar{\varphi}_c(z,t)$ and $\bar{\varphi}_f(z,t)$ for the crystalline and fluid particles, respectively.

## 3 Results and discussion

### 3.1 Qualitative observations

Experimental observations and simulations show heterogeneous crystal growth (Fig. 1). Initially, a very short induction period is observed. Then the crystal grows and the crystal–fluid interface moves into the fluid phase. The crystals mainly have an fcc, but also some hcp structure, indicating random stacking. At the wall as well as throughout the crystal, the (111) plane is oriented parallel to the wall with only a few defects and grain boundaries. Almost no crystalline particles are observed in the bulk; the few crystalline particles and small clusters formed by homogeneous nucleation in the bulk neither reach the size of a critical nucleus nor play a role in the propagation of the front or interfere with the depletion layer discussed below.

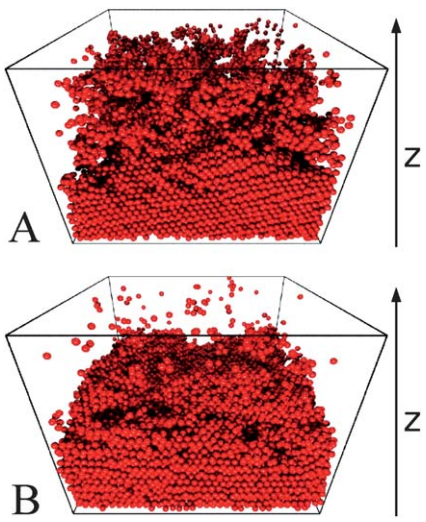


**Fig. 1** Snapshots based on (A) confocal microscopy and (B) simulations of a sample with volume fraction $\Phi = 0.52$ at time $t = 62\tau_B$. In this reconstruction, only crystalline particles are shown and the simulation box is reduced in the $z$ direction.

### 3.2 Development of the density profiles and formation of a depletion zone

The local volume fraction profiles $\varphi(z)$, based on both the experimental and simulation data, indicate the crystalline and fluid regions (Fig. 2A,C). The crystalline regions display characteristic maxima and minima reflecting an ordered structure. After formation, the crystals relax in the simulations. The spacing increases from the front, where it is $0.902\sigma$, to the wall ($z_0 = 0.921\sigma$), a value which is also reached at late times (Fig. 2C, inset). The spacing as well as the expansion does not depend on $\Phi$, with the relevant $\Phi$ all in the coexistence region. This slight expansion is in agreement with previous observations.[14,15,40,41] In the bulk of the crystal, the final equilibrium volume fraction is 0.545; Fig. 3 shows the locally-averaged volume fraction $\bar{\varphi}(z,t)$. The obtained local information allows us furthermore to distinguish crystalline and fluid particles (Fig. 2B,D). This

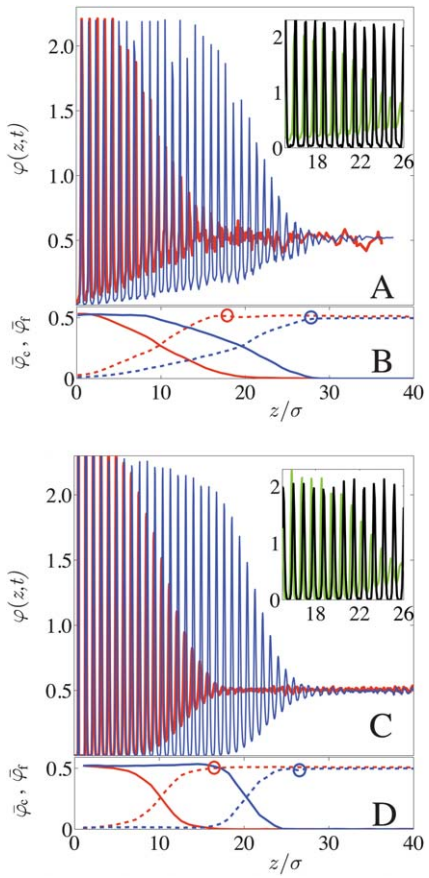


**Fig. 2** (A,C) Local volume fraction profile $\varphi(z)$ of all particles and (B,D) locally-averaged volume fraction profile $\bar{\varphi}_c(z)$ of crystalline (solid line) and $\bar{\varphi}_f(z)$ of fluid particles (dashed line) as a function of the reduced distance from the wall $z/\sigma$ at different times $t = 42\tau_B$ (red lines), $82\tau_B$ (blue lines), $102\tau_B$ (insets, green lines), $302\tau_B$ (insets, black lines). The data are obtained by (A,B) confocal microscopy and (C,D) simulations of a sample with volume fraction $\Phi = 0.52$. The circles indicate the location of the depletion zone (Fig. 3).

 

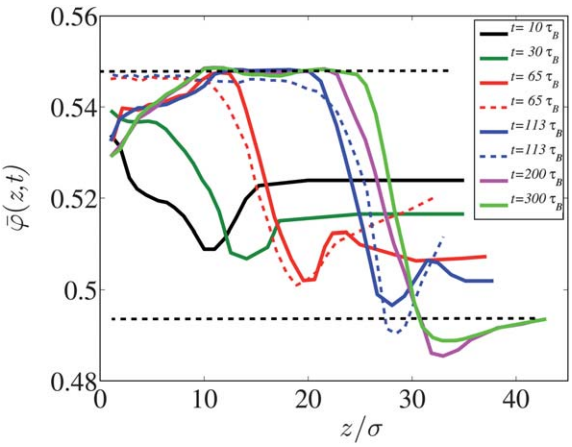


**Fig. 3** Locally-averaged volume fraction profile $\bar{\varphi}(z,t)$ of all particles as a function of the reduced distance from the wall $z/\sigma$ at different times $t/\tau_B$ (as indicated). The data are obtained by confocal microscopy (dashed lines) and simulations (solid lines) of a sample with volume fraction $\Phi = 0.52$. The horizontal dotted lines indicate the freezing and melting volume fractions.

indicates a volume fraction of fluid particles in the crystalline phase of a few percent which reflects the presence of defects and grain boundaries.

The bulk of the fluid appears disordered without pronounced fluctuations in the local volume fraction $\varphi(z)$ (Fig. 2A,C) consistent with only very few crystalline particles (Fig. 2B,D, solid lines). The locally-averaged volume fraction $\bar{\varphi}(z,t)$ shows a dependence on position $z$, time $t$ and bulk volume fraction $\Phi$ (Fig. 3; note the different $\bar{\varphi}$ range compared to Fig. 2B,D, which also shows the contributions of the crystal, $\bar{\varphi}_c$, and fluid, $\bar{\varphi}_f$, particles separately). In particular, we observe a depletion zone with a reduced volume fraction, in agreement with predictions.[14,41,42] The depletion zone is located in front of the crystal–fluid interface (Fig. 2B,D, circles) and extends over about $5\sigma$ and represents a dip in the volume fraction of about 0.01 (Fig. 3). For long times, where a stable interface position is achieved, the depletion zone disappears (Fig. 3, $t = 200\tau_B$ and $300\tau_B$). In the simulations, the volume fraction in the bulk of the fluid decreases with time due to the constant number of particles in the simulation box. Once this volume fraction drops below the freezing concentration, crystal growth ceases. In the experiments, the observation volume is embedded in a much larger reservoir and thus the volume fraction of the bulk fluid remains essentially constant.

The oscillations in the local volume fraction profile $\varphi(z)$ decay over a range of about 8 to 16 layers (Fig. 2A,C) as does the locally-averaged volume fraction $\bar{\varphi}(z,t)$ (Fig. 3), while a broader transition is experimentally observed if the crystalline, $\bar{\varphi}_c(z,t)$, and fluid, $\bar{\varphi}_f(z,t)$, particles are considered separately (Fig. 2B,D). The width of the crystal–fluid interface is consistent with previous theoretical, simulation and experimental studies.[18,43,44] Next to the crystal, we observe decreasing oscillations in $\varphi(z)$, which extend further in the $z$-direction than the crystalline particles (Fig. 2). This indicates layering of the fluid on the crystal surface, similar to the behaviour of fluids in the proximity of (structured) walls.

### 3.3 Front propagation and crystal growth

The evolution of the number of crystalline layers $N_c(t)/N_1$ is determined from the total number of crystalline particles $N_c(t)$ and the mean number of crystalline particles in a single layer $N_1$ (Fig. 4). Similar results are obtained based on the propagation of the crystal–fluid interface, $z_c(t)$, whose location is approximated by the position where the locally-averaged volume fractions of crystalline and fluid particles are identical (Fig. 2B,D, represented as dash-dotted lines in Fig. 4, inset) as well as by the progression of the envelope of $\varphi(z)$ (Fig. 2A,C, represented as dashed lines in Fig. 4, inset). The simulations are performed with monodisperse particles, in contrast to the experiments. This is justified by the minor effect of small polydispersities on crystal growth; additional simulations of particles with a polydispersity of 5% result only in a modest decrease of the growth velocity compared to the monodisperse case (Fig. 4, inset).

Whereas crystallization of the first few layers takes about $5\tau_B$ in the simulations, it is almost instantaneous in the experiments due to the initial crystalline layer. After this initial stage, for an extended period there is a rapid increase in the number of crystalline particles $N_c(t)$, first linearly and then sub-linearly (Fig. 4). At very long times, growth seems to considerably slow down or even cease. In the simulations this occurs when the volume fraction of the fluid drops below 0.494 and is due to the fixed number of particles in a simulation box of finite size. In the experiments the volume fraction of the fluid is essentially constant due to the large reservoir. Nevertheless, when the observation volume is completely filled with crystalline particles growth apparently saturates.

We determine the growth velocity $v = (\tau_B/N_1)\mathrm{d}N_c/\mathrm{d}t$ during the linear part of the time dependence of $N_c(t)/N_1$. In the experiments, the growth velocity $v(\Phi)$ displays a maximum at a bulk volume fraction $\Phi = 0.52$ (Fig. 5, open squares). The simulations

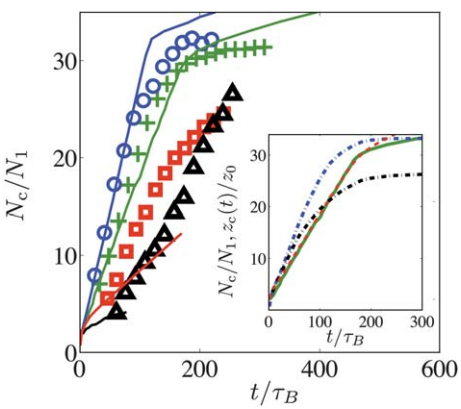


**Fig. 4** Number of crystalline layers $N_c(t)/N_1$ as a function of reduced time $t/\tau_B$. Samples with different bulk volume fractions $\Phi = 0.50$ (□), 0.52 (+) 0.53 (○), 0.545 (△) have been investigated by confocal microscopy (symbols) and simulations (lines of same colour). The inset shows differently analyzed simulation results of the sample with $\Phi = 0.52$: number of crystalline layers $N_c(t)/N_1$ (—), crystal–fluid interface position $z_c(t)/z_0$ defined as the position where the locally-averaged volume fractions of crystalline and fluid particles are identical (- - -) and based on the lower envelope of $\varphi(z)$ (- - -). The inset includes simulation results for particles with a polydispersity of 5% (black - - -).

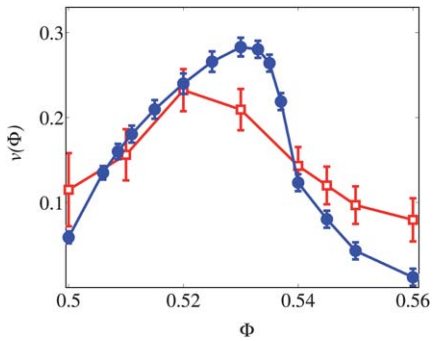


**Fig. 5** (A) Growth velocity $v(\Phi)$ as a function of bulk volume fraction $\Phi$ as determined by confocal microscopy (□) and simulations (●). The lines are guides to the eye.



yield qualitatively similar behaviour and very comparable growth velocities, but the maximum is shifted to a larger bulk volume fraction, $\Phi = 0.53$, and the decrease toward larger $\Phi$ is more pronounced (closed circles). This might be due to the slightly different situation in the experiments and simulations with a constant liquid volume fraction and a fixed total number of particles and thus a decreasing liquid volume fraction, respectively (Fig. 3). The maximum in $v(\Phi)$ at $\Phi \approx 0.53$ is in agreement with previous studies.[1,14,15,40,41] It is thought to be due to the interplay between the increasing thermodynamic driving force and the decreasing mobility. The diffusion coefficient observed in our simulations and experiments[45] indeed decreases with increasing bulk volume fraction $\Phi$. This slowing down results from progressive caging.[45] It dominates at large $\Phi$, while the increasing thermodynamic driving force[46] determines the behaviour of the growth velocity $v(\Phi)$ at small $\Phi$.

## 4 Conclusions

Using confocal microscopy and Brownian dynamics simulations, we investigated heterogeneous crystallization on an individual particle level. We followed the evolution of the density profiles inside the crystal and fluid as well as the advancing crystal–fluid interface. We observe a slight expansion of the crystal and a width of the crystal–fluid interface which is consistent with previous reports.[14,15,18,40,41,43,44] Next to the crystal, the fluid is found to be layered with decreasing density fluctuations. Furthermore, microscopic information on the growth velocity is obtained, which shows non-monotonic behaviour with a maximum at a bulk volume fraction $\Phi \approx 0.53$. Importantly, in the experiments and simulations we directly observe a depletion layer in front of the advancing crystal–fluid interface. The depletion zone is indicated by a reduction in the local volume fraction of about 0.01 and extends over about five particle diameters. It disappears when a stable interface position is reached.

## 5 Acknowledgement

We thank T. Palberg (Mainz), C.P. Royall (Bristol) and R.P.A. Dullens (Oxford) for helpful discussions, A.B. Schofield (Edinburgh) for supplying the PMMA particles, and C. Seidel (Düsseldorf, Centre for Advanced Imaging) for providing time on the confocal microscope. This work was supported by the DFG (SPP 1296). E.A. was partially supported by the US Department of Energy under grant (DE-FG02-05ER46244).

## References

1 T. Palberg, *J. Phys.: Condens. Matter*, 1999, **11**, R323.
2 U. Gasser, *J. Phys.: Condens. Matter*, 2009, **21**, 203101.
3 P. Wette, A. Engelbrecht, R. Salh, I. Klassen, D. Menke, D. M. Herlach, S. V. Roth and H. J. Schöpe, *J. Phys.: Condens. Matter*, 2009, **21**, 464115.
4 G. Kahl and H. Löwen, *J. Phys.: Condens. Matter*, 2009, **21**, 464101.
5 J. Yamanaka, M. Murai, Y. Iwayama, M. Yonese, K. Ito and T. Sawada, *J. Am. Chem. Soc.*, 2004, **126**, 7156.
6 H. Emmerich, K. Binder and B. Nestler, *Phil. Mag. Lett.*, 2007, **87**, 791.
7 N. V. Dziomkina and G. J. Vancso, *Soft Matter*, 2005, **1**, 265.
8 W. C. K. Poon, S. U. Egelhaaf, P. A. Beales, A. Salonen and L. Sawyer, *J. Phys.: Condens. Matter*, 2000, **12**, L569.
9 M. C. Wiener, *Methods*, 2004, **34**, 364.
10 H. Sedgwick, K. Kroy, A. Salonen, M. B. Robertson, S. U. Egelhaaf and W. C. K. Poon, *Eur. Phys. J. E*, 2005, **16**, 77.
11 E. H. Snell and J. R. Helliwell, *Rep. Prog. Phys.*, 2005, **68**, 799.
12 R. P. Sear, *J. Phys.: Condens. Matter*, 2007, **19**, 033101.
13 H. Sedgwick, J. E. Cameron, W. C. K. Poon and S. U. Egelhaaf, *J. Chem. Phys.*, 2007, **127**, 125102.
14 B. J. Ackerson and K. Schätzel, *Phys. Rev. E: Stat. Phys., Plasmas, Fluids, Relat. Interdiscip. Top.*, 1995, **52**, 6448.
15 J. L. Hartland and W. van Megen, *Phys. Rev. E: Stat. Phys., Plasmas, Fluids, Relat. Interdiscip. Top.*, 1997, **55**, 3054.
16 T. Schilling, H. J. Schöpe, M. Oettel, G. Opletal and I. Snook, *Phys. Rev. Lett.*, 2010, **105**, 025701.
17 U. Gasser, E. R. Weeks, A. Schofield, P. N. Pusey and D. A. Weitz, *Science*, 2001, **292**, 258.
18 R. P. A. Dullens, D. G. A. L. Aarts and W. K. Kegel, *Phys. Rev. Lett.*, 2006, **97**, 228301.
19 C. P. Royall, C. Patrick, S. R. Williams, R. Stephen, T. Ohtsuka and H. Tanaka, *Nat. Mater.*, 2008, **7**, 556.
20 L. Assoud, F. Ebert, P. Keim, R. Messina, G. Maret and H. Löwen, *Phys. Rev. Lett.*, 2009, **102**, 238301.
21 S. Auer and D. Frenkel, *Adv. Polym. Sci.*, 2005, **173**, 149.
22 H. Shintani and H. Tanaka, *Nat. Phys.*, 2006, **2**, 200.
23 A. Cacciuto and D. Frenkel, *Phys. Rev. E: Stat., Nonlinear, Soft Matter Phys.*, 2005, **72**, 041604.
24 M. Heni and H. Löwen, *Phys. Rev. Lett.*, 2000, **85**, 3668.
25 W. S. Xu, Z. Y. Sun and L. J. An, *J. Chem. Phys.*, 2010, **132**, 144506.
26 A. Cacciuto, A. Auer and D. Frenkel, *Nature*, 2004, **428**, 404.
27 V. W. A. de Villeneuve, D. Verboekend, R. P. A. Dullens, D. G. A. L. Aarts, W. K. Kegel and H. N. W. Lekkerkerker, *J. Phys.: Condens. Matter*, 2005, **17**, S3371.
28 V. W. A. de Villeneuve, R. P. A. Dullens, D. G. A. L. Aarts, E. Groeneveld, J. H. Scherff, W. K. Kegel and H. N. W. Lekkerkerker, *Science*, 2005, **309**, 1231.
29 S. van Teeffelen, C. N. Likos and H. Löwen, *Phys. Rev. Lett.*, 2008, **100**, 108302.
30 K. H. Lin, J. C. Crocker, V. Prasad, A. Schofield, D. A. Weitz, T. C. Lubensky and A. G. Yodh, *Phys. Rev. Lett.*, 2000, **85**, 1770.
31 J. P. Hoogenboom, A. K. van Langen-Suurling, J. Romijn and A. van Blaaderen, *Phys. Rev. E: Stat., Nonlinear, Soft Matter Phys.*, 2004, **69**, 051602.
32 M. Heni and H. Löwen, *Phys. Rev. E: Stat. Phys., Plasmas, Fluids, Relat. Interdiscip. Top.*, 1999, **60**, 7057.
33 S. Auer and D. Frenkel, *Phys. Rev. Lett.*, 2003, **91**, 015703.
34 W. Schaertl and H. Sillescu, *J. Stat. Phys.*, 1994, **77**, 1007.
35 M. C. Jenkins and S. U. Egelhaaf, *Adv. Colloid Interface Sci.*, 2008, **136**, 65.
36 J. C. Crocker and D. G. Grier, *J. Colloid Interface Sci.*, 1996, **179**, 298.
37 B. Cichocki and K. Hinsen, *Phys. A*, 1990, **166**, 473.
38 P. J. Steinhardt, D. R. Nelson and M. Ronchetti, *Phys. Rev. B*, 1983, **28**, 784.
39 P. R. ten Wolde, M. J. Ruiz-Montero and D. Frenkel, *Phys. Rev. Lett.*, 1995, **75**, 2714.

 

40 H. J. Schöpe, G. Bryant and W. van Megen, *J. Chem. Phys.*, 2007, **127**, 084505.
41 N. M. Dixit and C. F. Zukoski, *Phys. Rev. E: Stat. Phys., Plasmas, Fluids, Relat. Interdiscip. Top.*, 2001, **64**, 041604.
42 S. Derber, T. Palberg, K. Schätzel and J. Vogel, *Phys. A*, 1997, **235**, 204.
43 R. L. Davidchack and B. B. Laird, *J. Chem. Phys.*, 1998, **108**, 9452.
44 T. Zykova-Timan, J. Horbach and K. Binder, *J. Chem. Phys.*, 2010, **133**, 014705.
45 P. N. Pusey, in: J. P. Hansen, D. Levesque, J. Zinn-Justin (ed.) *Liquids, Freezing and Glass Transition*, Elsevier Science Publishers (1991).
46 P. N. Pusey, E. Zaccarelli, C. Valeriani, E. Sanz, W. C. K. Poon and M. E. Cates, *Philos. Trans. R. Soc. London, Ser. A*, 2009, **367**, 4993.